An Innovative Multi-Frequency PSO-Based Method for the Microwave Imaging of Buried Objects having Different Conductivities

M. Salucci, L. Poli, N. Anselmi, and A. Massa

Abstract

In this work, an innovative particle swarm optimization (*PSO*)-based microwave imaging approach is presented to solve the subsurface inverse scattering problem. The proposed *MF-IMSA-PSO* method integrates a customized *PSO* solver within a multi-scaling technique (i.e., the *IMSA*) in order to limit the ratio between problem unknowns and non-redundant data, mitigating the negative effects of both non-linearity and ill-posedness through the exploitation of progressively *acquired* information about the solution. Moreover, the inversion is performed by considering a multi-frequency (*MF*) solution strategy, by jointly processing several frequency components extracted from the spectrum of the measured data through ground penetrating radar (*GPR*). Some numerical results are shown in order to verify the effectiveness of the developed GPR microwave imaging technique when dealing with objects having a conductivity different from that of the hosting (lossy) soil.

1 Definitions

1.1 Glossary

- SF: Single-Frequency;
- FH: Frequency-Hopping;
- MF: Multi-Frequency;
- P: Swarm dimension;
- U: Total number of unknowns;
- S: Maximum number of $IMSA$ zooming steps;
- s^{best}: Last performed $IMSA$ zooming step ($s^{best} \leq S$);
- η_{th}: $IMSA$ zooming threshold;
- D_{inv}: Investigation domain;
- D_{obs}: Observation domain;
- L: Side of the investigation domain;
- N: Number of discretization cells in D_{ind};
- V: Number of views;
- M: Number of measurement points;
- F: Number of frequencies considered for the inversion;
- $\mathbf{r}^{(v)} = \left(x^{(v)}, y^{(v)}\right)$: Coordinates of the v-th source ($v = 1, \ldots, V$).
- $\mathbf{r}_m^{(v)} = \left(x_m^{(v)}, y_m^{(v)}\right)$: Coordinates of the m-th measurement point for the v-th view v, ($m = 1, \ldots, M$);
- $\varepsilon_{ra} = \frac{\varepsilon_a}{\varepsilon_0}$: Relative electric permittivity for the upper half-space ($y > 0$);
- σ_a: Conductivity for the upper half-space ($y > 0$);
- $\varepsilon_{rb} = \frac{\varepsilon_b}{\varepsilon_0}$: Background relative electric permittivity;
- σ_b: Background conductivity;
- $E_{inc}^{(v)}(\mathbf{r}_n; f)$: Measured internal incident field inside the n-th cell, for the v-th view at frequency f;
- $\widetilde{E}_{inc}^{(v)}(\mathbf{r}_n; f)$: Computed internal incident field inside the n-th cell, for the v-th view at frequency f;
- $E_{scatt}^{(v)}\left(\mathbf{r}_m^{(v)}; f\right)$: Measured external scattered by the m-th measurement point, for the v-th view at frequency f;
- $\widetilde{E}_{scatt}^{(v)}\left(\mathbf{r}_m^{(v)}; f\right)$: Measured external scattered by the m-th measurement point, for the v-th view at frequency f.

1.2 Contrast function

The contrast function at frequency f is defined as

$$\tau(\mathbf{r}; f) = \frac{\varepsilon_{eq}(\mathbf{r}) - \varepsilon_{eqb}}{\varepsilon_0} = [\varepsilon_r(\mathbf{r}) - \varepsilon_{rb}] + j\left[\frac{\sigma_b - \sigma(\mathbf{r})}{2\pi f \varepsilon_0}\right]$$

where

- $\mathbf{r} = (x, y)$: position vector;
- $\Re\{\tau(\mathbf{r}; f)\} = [\varepsilon_r(\mathbf{r}) - \varepsilon_{rb}]$;
- $\Im\{\tau(\mathbf{r}; f)\} = \left[\frac{\sigma_b - \sigma(\mathbf{r})}{2\pi f \varepsilon_0}\right]$;
- $\varepsilon_{eq}(\mathbf{r}) = \varepsilon_0 \varepsilon_r(\mathbf{r}) - j\frac{\sigma(\mathbf{r})}{2\pi f}$;
- $\varepsilon_{eqb} = \varepsilon_0 \varepsilon_{rb} - j\frac{\sigma_b}{2\pi f}$;
- $\varepsilon_r(\mathbf{r})$: relative electric permittivity at position $\mathbf{r}$;
- $\sigma(\mathbf{r})$: conductivity at position $\mathbf{r}$;

NOTE: we assume that $\varepsilon_r(\mathbf{r})$ and $\sigma(\mathbf{r})$ are **not frequency dependent** (non-dispersive mediums).

1.2.1 Contrast function and reference frequency f_{ref} (MF approaches)

The contrast function at a generic frequency f can be expressed by means of the contrast function computed for a selected reference frequency

$$f = f_{ref} \tag{1}$$

as follows

$$\tau(\mathbf{r}; f) = \Re\{\tau(\mathbf{r}; f_{ref})\} + j\frac{f_{ref}}{f}\Im\{\tau(\mathbf{r}; f_{ref})\}. \tag{2}$$

This allows to reduce the number of unknowns when dealing with multi-frequency techniques, since we can just consider the contrast function at the reference frequency.

1.3 Cost function & unknowns

1.3.1 Multi-Frequency (MF) approaches

These approaches jointly consider data at F frequencies. The functional minimized by the inversion algorithm is defined as

$$\Phi\left(\mathbf{x}\right)=\Phi_{state}\left(\mathbf{x}\right)+\Phi_{data}\left(\mathbf{x}\right) \tag{3}$$

where $\Phi_{state}\left(\mathbf{x}\right)$ and $\Phi_{data}\left(\mathbf{x}\right)$ are respectively the data and state terms of the cost function, defined as

$$\Phi_{state}\left(\mathbf{x}\right)=\frac{\sum_{j=1}^{F}\sum_{v=1}^{V}\sum_{n=1}^{N}\left|E_{inc}^{(v)}\left(\mathbf{r}_n;f_j\right)-\widetilde{E}_{inc}^{(v)}\left(\mathbf{r}_n;f_j\right)\right|^2}{\sum_{j=1}^{F}\sum_{v=1}^{V}\sum_{n=1}^{N}\left|E_{inc}^{(v)}\left(\mathbf{r}_n;f_j\right)\right|^2} \tag{4}$$

$$\Phi_{data}=\frac{\sum_{j=1}^{F}\sum_{v=1}^{V}\sum_{m=1}^{M}\left|E_{scatt}^{(v)}\left(\mathbf{r}_m^{(v)};f_j\right)-\widetilde{E}_{scatt}^{(v)}\left(\mathbf{r}_m^{(v)};f_j\right)\right|^2}{\sum_{j=1}^{F}\sum_{v=1}^{V}\sum_{m=1}^{M}\left|E_{scatt}^{(v)}\left(\mathbf{r}_m^{(v)};f_j\right)\right|^2} \tag{5}$$

The unknowns of the inversion problem are

$$\mathbf{x}=\left\{\tau\left(\mathbf{r};f_{ref}\right);E_{tot}^{(v)}\left(\mathbf{r}_n;f_j\right)\right\}\qquad n=1,...,N;v=1,...,V;j=1,...,F. \tag{6}$$

The total number of unknowns for MF-based approaches is then given by

$$U_{MF}=2N\left(1+VF\right). \tag{7}$$

1.4 Reconstruction errors

The following integral error is defined

$$\Xi_{reg}=\frac{1}{N_{reg}}\sum_{n=1}^{N_{reg}}\frac{\left|\tau_n^{act}-\tau_n^{rec}\right|}{\left|\tau_n^{act}+1\right|} \tag{8}$$

where reg indicates if the error computation covers

- the overall investigation domain ($reg \Rightarrow tot$),
- the actual scatterer support ($reg \Rightarrow int$),
- or the background region ($reg \Rightarrow ext$).

2 Numerical Results: Variation of the Object Conductivity

2.1 $\mathcal{I}$-Shaped object ($\varepsilon_{r,obj} = 5.5$)

2.1.1 Parameters

Background

Inhomogeneous and nonmagnetic background composed by two half spaces

- Upper half space ($y > 0$ - air): $\varepsilon_{ra} = 1.0$, $\sigma_a = 0.0$;
- Lower half space ($y < 0$ - soil): $\varepsilon_{rb} = 4.0$, $\sigma_b = 10^{-3}$[S/m];

Investigation domain (D_{inv})

- Side: $L_{D_{inv}} = 0.8$ [m];
- Barycenter: $\left(x_{bar}^{D_{inv}}, y_{bar}^{D_{inv}}\right) = (0.00, -0.4)$ [m];

Time-Domain forward solver ($FDTD$ - $GPRMax2D$)

- Side of the simulated domain: $L = 6$ [m];
- Number of cells: $N^{FDTD} = 750 \times 750 = 5.625 \times 10^5$;
- Side of the $FDTD$ cells $l^{FDTD} = 0.008$ [m];
- Simulation time window: $T^{FDTD} = 20 \times 10^{-9}$ [sec];
- Time step: $\Delta t^{FDTD} = 1.89 \times 10^{-11}$ [sec];
- Number of time samples: $N_t^{FDTD} = 1060$;
- Boundary conditions: perfectly matched layer (PML);
- Source type: Gaussian mono-cycle (first Gaussian pulse derivative, called "Ricker" in $GPRMax2D$)
  - Central frequency: $f_0 = 300$ [MHz];
  - Source amplitude: $A = 1.0$ [A];

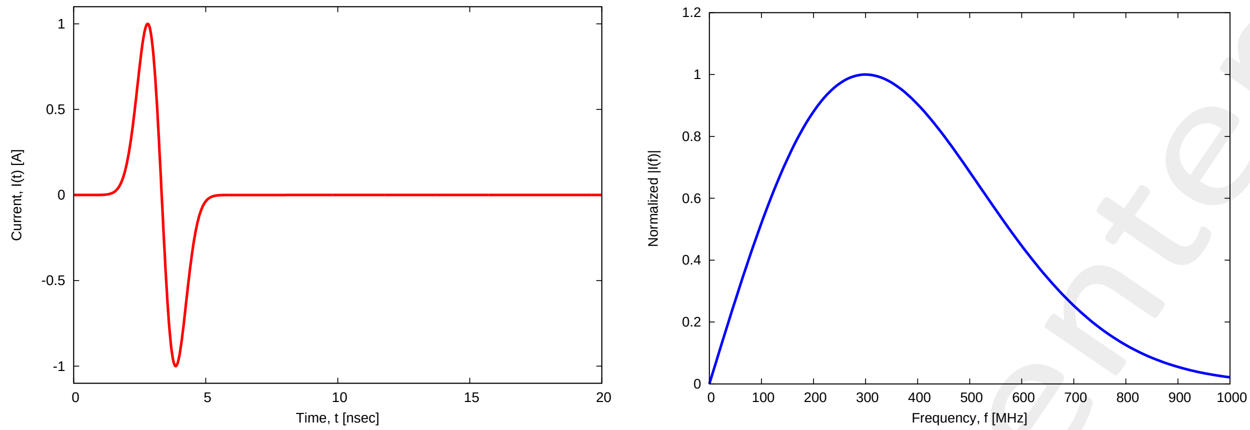

(a) (b)

Figure 1: *GPRMax2D* excitation signal. (a) Time pulse, (b) normalized frequency spectrum.

Frequency parameters

- Frequency range: $f \in [f_{min}, f_{max}] = [200.0, 600.0]$ [MHz] (-3 [dB] bandwidth of the Gaussian Monocycle excitation centered at $f_0 = 300$ [MHz]);
- Frequency step: $\Delta f = 100$ [MHz] ($F = 5$ frequency steps in $[f_{min}, f_{max}]$);

f [MHz]	λ_a [m]	λ_b [m]	f^* [MHz]
200.0	1.50	0.75	200.5
300.0	1.00	0.50	297.6
400.0	0.75	0.37	401.1
500.0	0.60	0.30	498.1
600.0	0.50	0.25	601.6

Table 1: Considered frequencies and corresponding wavelength in the upper medium (λ_a, free space) and in the lower medium (λ_b, soil). f^* is the nearest frequency sample available from transformed time-domain data, and represents the real frequency considered by the inversion algorithm.

Scatterer

- Type: $\mathcal{I}$-Shaped;
- Side: 0.28 [m];
- Electromagnetic properties: $\varepsilon_{r,obj} = 5.5$, $\sigma_{obj} = \left\{10^{-4}; 5\times10^{-4}; 10^{-3}; 5\times10^{-3}; 10^{-2}\right\}$ [S/m];

$\varepsilon_{r,obj}$	σ_{obj} [S/m]	$\Re\{\tau\}$	$\Im\{\tau\}$
5.5	10^{-4}	1.5	0.040
5.5	5×10^{-4}	1.5	0.022
5.5	10^{-3}	1.5	0.000
5.5	5×10^{-3}	1.5	-0.180
5.5	10^{-2}	1.5	-0.404

Table 2: Real and imaginary parts of the contrast function vs. different values of object conductivity. The imaginary part is computed as $\Im\{\tau\} = \left[\frac{\sigma_b - \sigma_{obj}}{2\pi f \varepsilon_0}\right]$ at the central frequency ($f_{cent} = 400$ [MHz]).

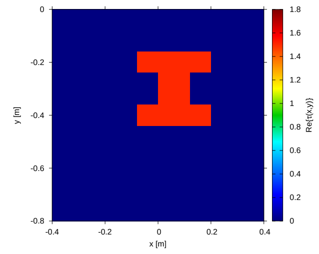

$(a)\ \Re\{\tau\}$

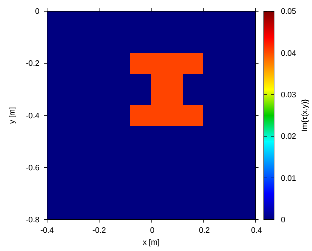

$(b)\ \Im\{\tau\}$ - $\sigma_{obj} = 10^{-4}$[S/m]

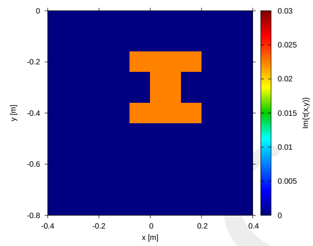

$(c)\ \Im\{\tau\}$ - $\sigma_{obj} = 5 \times 10^{-4}$[S/m]

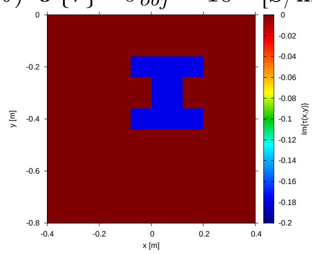

$(d)\ \Im\{\tau\}$ - $\sigma_{obj} = 5 \times 10^{-3}$[S/m]

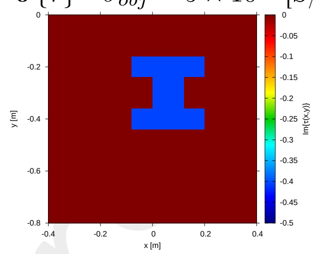

$(e)\ \Im\{\tau\}$ - $\sigma_{obj} = 10^{-2}$[S/m]

Figure 2: Actual object.

Measurement setup

- Considered frequency: $f_{min} = 200$ [MHz], $\lambda_b = 0.75$ [m]. [1]
- $\#DoFs = 2ka = \frac{2\pi}{\lambda_b} L\sqrt{2} = \frac{2\pi}{0.75} 0.8\sqrt{2} \simeq 9.5$;
- Number of views (sources): $V = 10$;
  - $\min\{x_v\} = -0.5$ [m], $\max\{x_v\} = 0.5$ [m];
  - height: $y_v = 0.1$ [m], $\forall v = 1, \dots, V$;
- Number of measurement points: $M = 9$;
  - $\min\{x_m\} = -0.5$ [m], $\max\{x_m\} = 0.5$ [m];
  - height: $y_m = 0.1$ [m], $\forall m = 1, \dots, M$;

[1] **NOTE:** This choice is done in order to keep the number of unknowns lower than 5000.

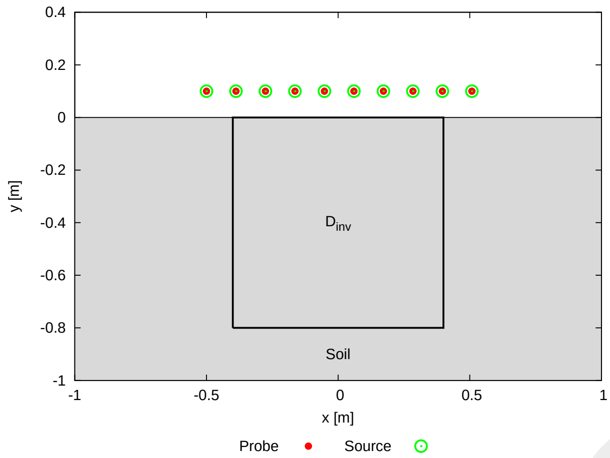

Figure 3: Location of the measurement points ($M = 9$) and of the sources ($V = 10$). Only one source is active for each view.

Inverse solver parameters

- **Shared parameters**
  - Number of unknowns: $U = 2N(1 + VF) = 4998$;
  - Weight of the state term of the functional: 1.0;
  - Weight of the data term of the functional: 1.0;
  - Weight of the penalty term of the functional: 0.0;
  - Convergence threshold: 10^{-10};
  - Variable ranges:
    - $\varepsilon_r \in [4.0, 5.8]$;
    - $\Re\left\{E_{tot}^{int}\right\} \in [-8, 8]$, $\Im\left\{E_{tot}^{int}\right\} \in [-8, 8]$;
  - Degrees of freedom:
    - Considered frequency: $f_{min} = 200$ [MHz], $\lambda_b = 0.75$ [m];
    - $\frac{(2ka)^2}{2} = \frac{\left(2\times\frac{2\pi}{\lambda_b}\times\frac{L\sqrt{2}}{2}\right)^2}{2} = 4\pi^2\left(\frac{L}{\lambda_b}\right)^2 = 4\pi^2\left(\frac{0.8}{0.75}\right)^2 \simeq 44.87$;
  - Number of cells: $N = 49 = 7 \times 7$;
  - Maximum number of $IMSA$ steps: $S = 4$;
  - Side ratio threshold: $\eta_{th} = 0.2$;
- $MF - IMSA - PSO$ **parameters**
  - Maximum number of iterations: $I = 20000$;
  - Swarm dimension: $P = \frac{5}{100} \times U = 250$;
  - $C_1 = C_2 = 2.0$;
  - Inertial weight: $w = 0.4$;

- Velocity clamping: enabled;

- $MF - IMSA - CG$ **parameters**
  - Maximum number of iterations: $I = 200$;

Signal to noise ratio (on $E_{tot}(t)$)

- $SNR = \{50, 40, 30, 20\}$ [dB] + Noiseless data.

2.1.2 $\sigma_{obj} = 10^{-4}$ [S/m] ($\Im\{\tau\} = 0.040$) - $MF-IMSA-PSO$ vs. $MF-IMSA-CG$: Final reconstructions

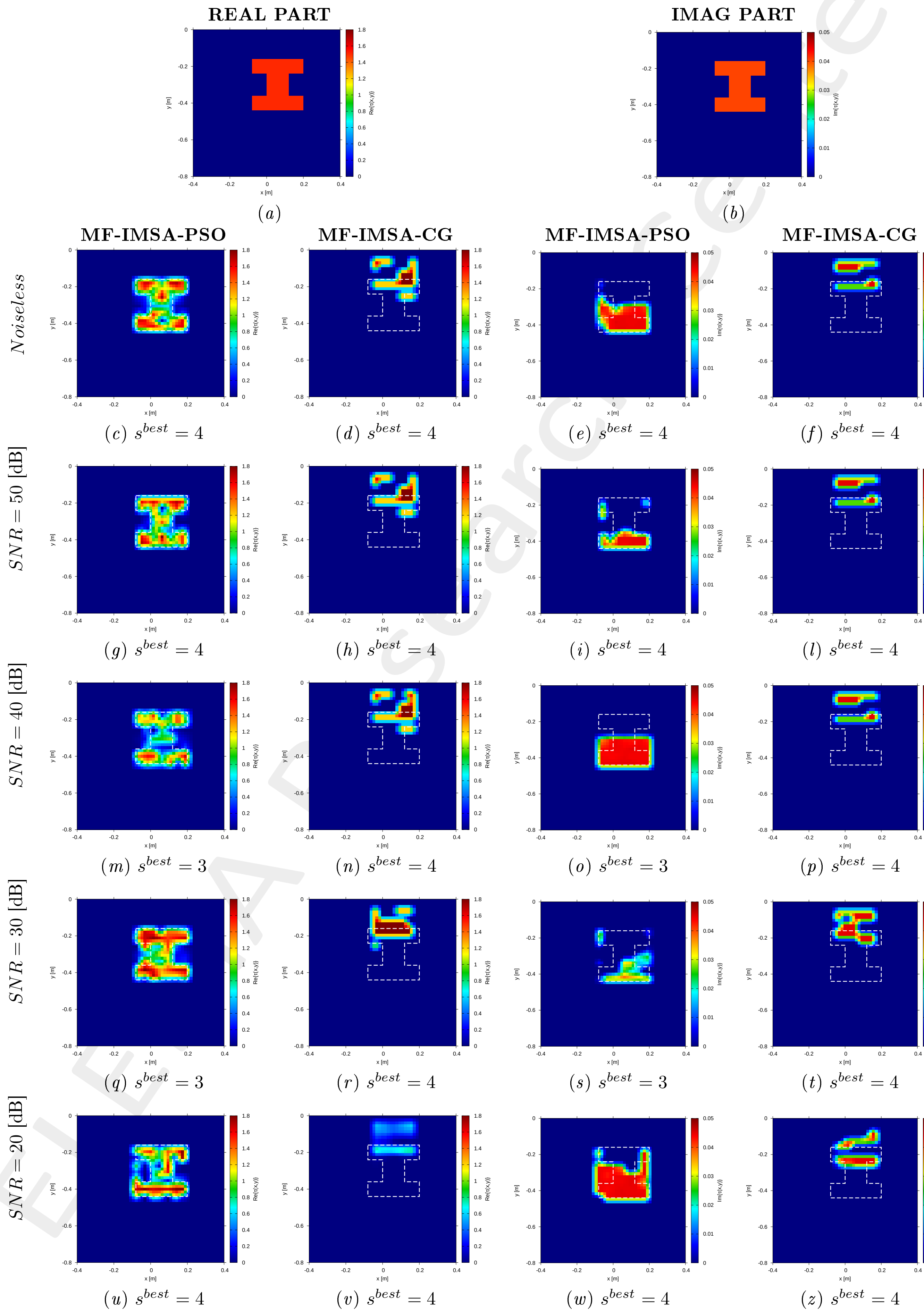

Figure 4: $MF-IMSA-PSO$ vs. $MF-IMSA-CG$: Retrieved dielectric profiles at the $IMSA$ convergence

2.1.3 $\sigma_{obj} = 5 \times 10^{-4}$ [S/m] ($\Im\{\tau\} = 0.022$) - $MF-IMSA-PSO$ vs. $MF-IMSA-CG$: Final reconstructions

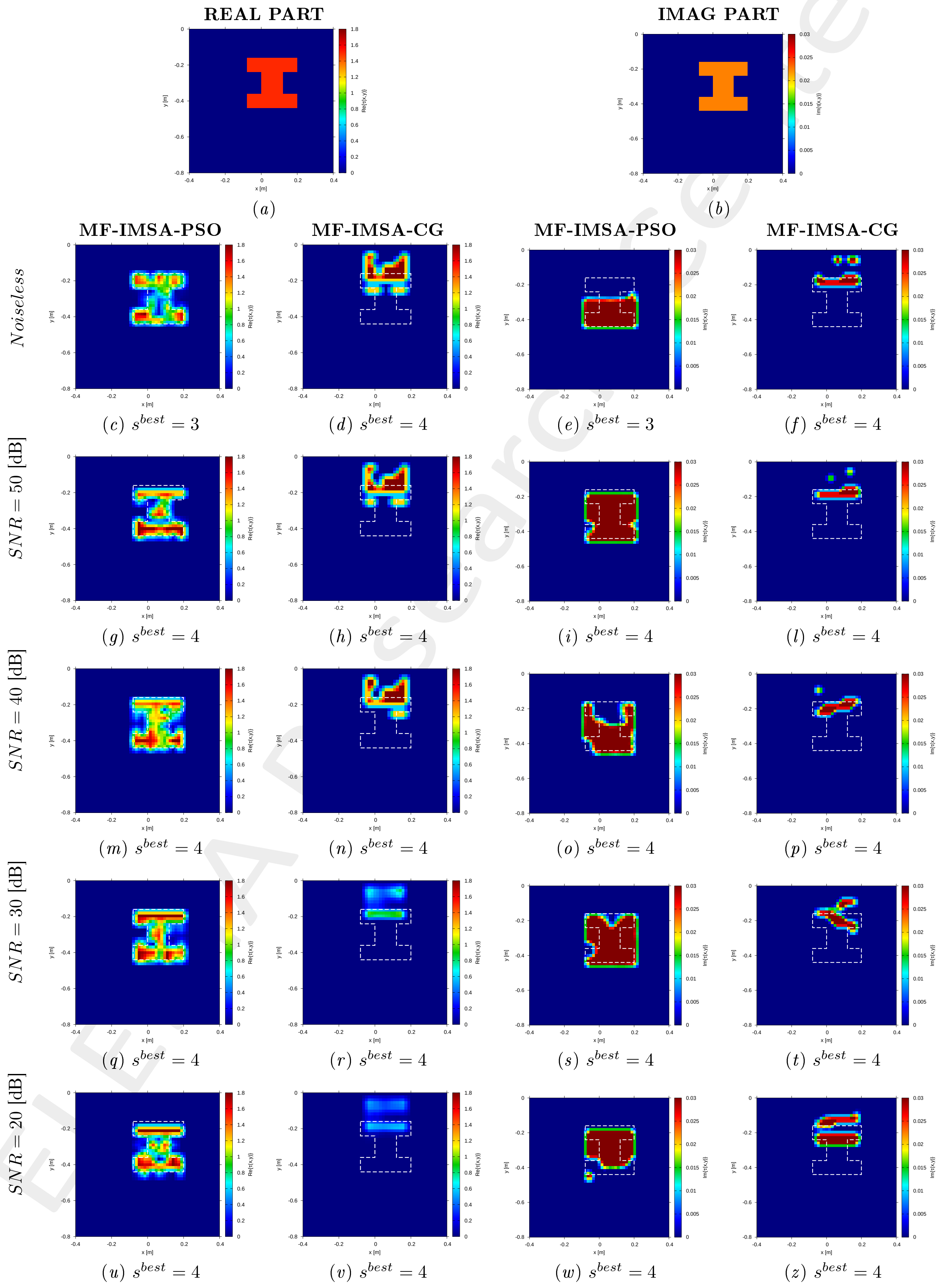

Figure 5: $MF-IMSA-PSO$ vs. $MF-IMSA-CG$: Retrieved dielectric profiles at the $IMSA$ convergence

2.1.4 $\sigma_{obj} = 10^{-3}$ [S/m] ($\Im\{\tau\} = 0.0$) - $MF-IMSA-PSO$ vs. $MF-IMSA-CG$: Final reconstructions

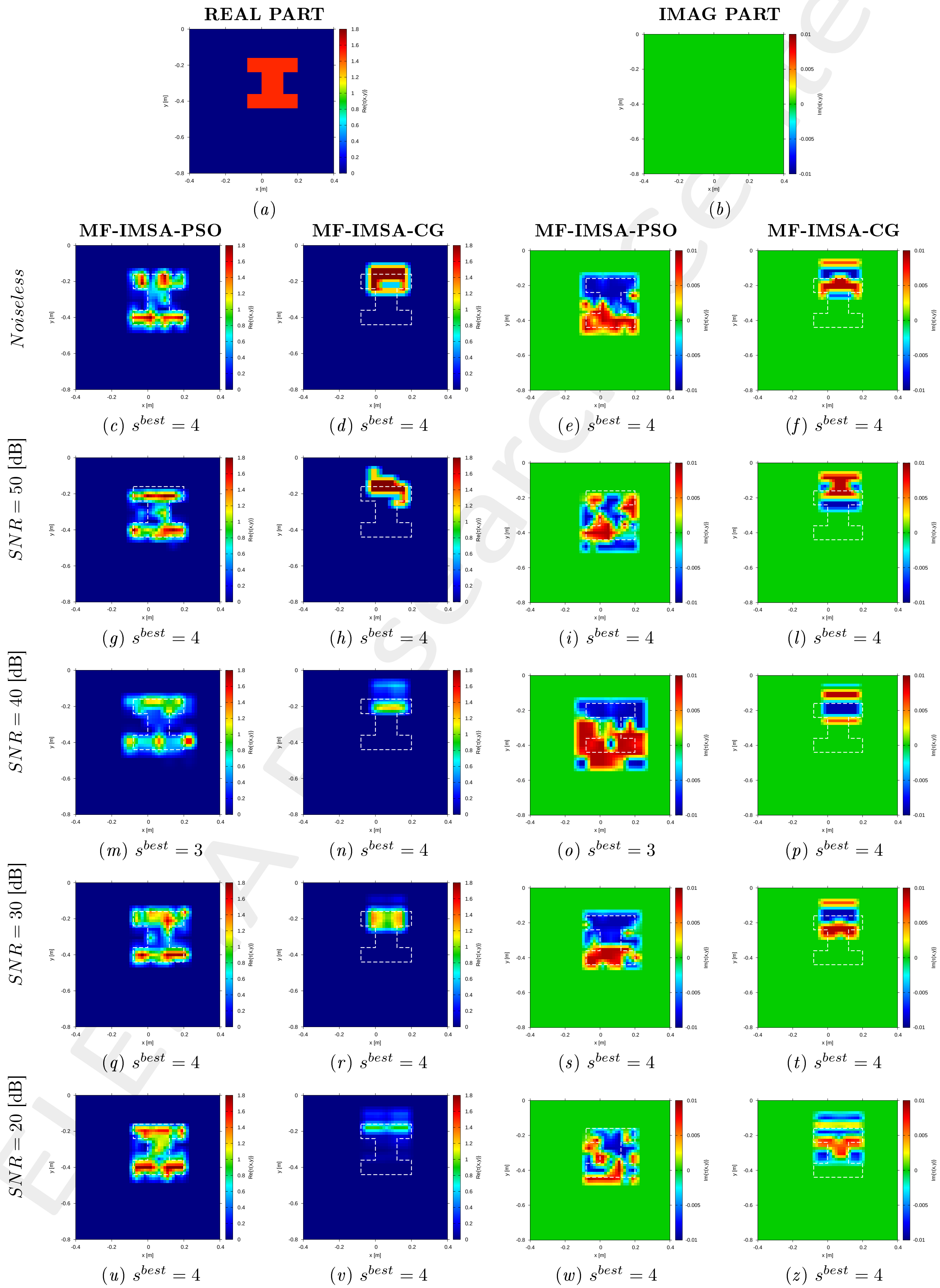

Figure 6: $MF-IMSA-PSO$ vs. $MF-IMSA-CG$: Retrieved dielectric profiles at the $IMSA$ convergence

2.1.5 $\sigma_{obj} = 5 \times 10^{-3}$ [S/m] ($\Im\{\tau\} = -0.180$) - $MF-IMSA-PSO$ vs. $MF-IMSA-CG$: Final reconstructions

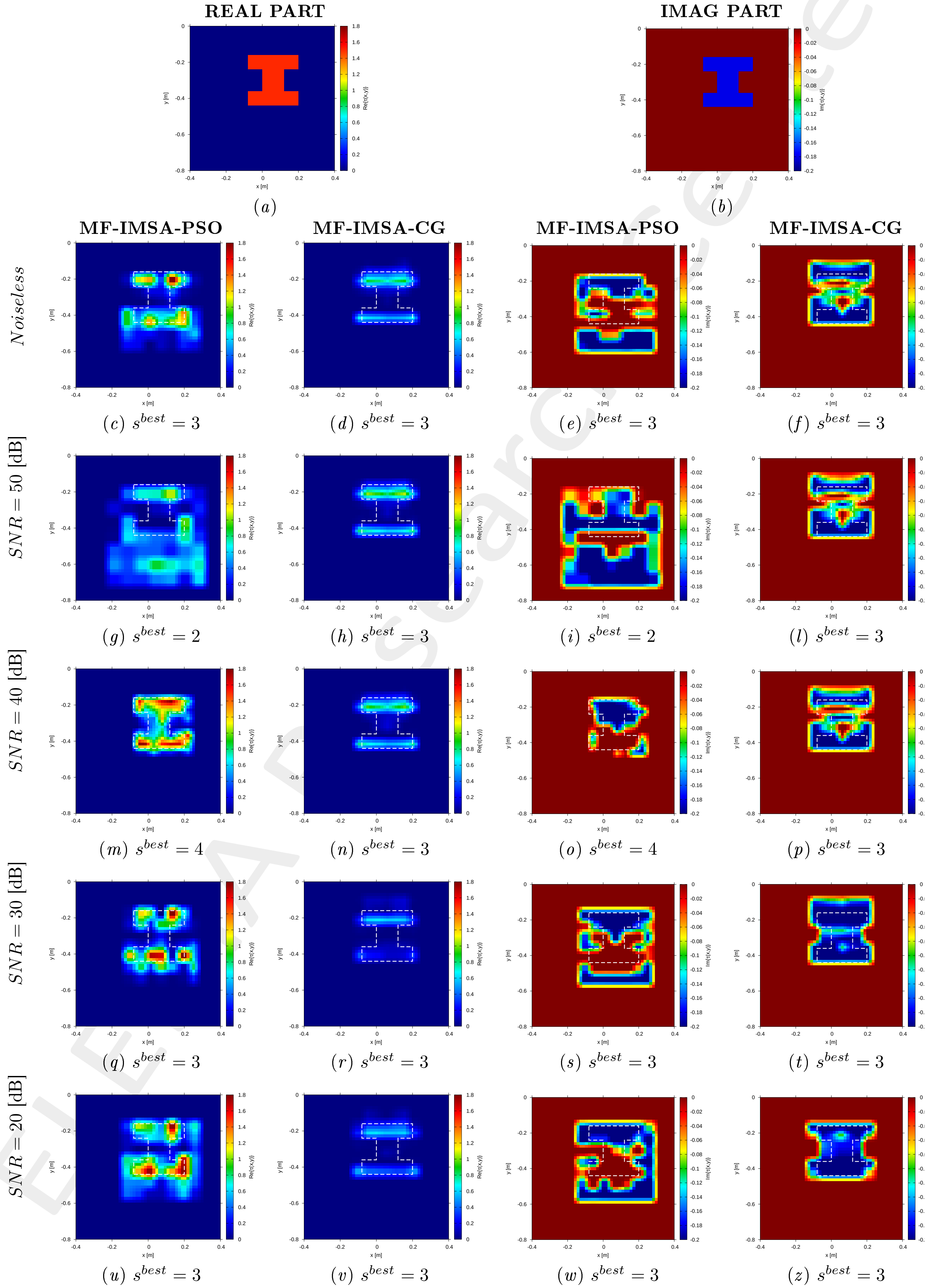

Figure 7: $MF-IMSA-PSO$ vs. $MF-IMSA-CG$: Retrieved dielectric profiles at the $IMSA$ convergence

2.1.6 $\sigma_{obj} = 10^{-2}$ [S/m] ($\Im\{\tau\} = -0.404$) - $MF-IMSA-PSO$ vs. $MF-IMSA-CG$: Final reconstructions

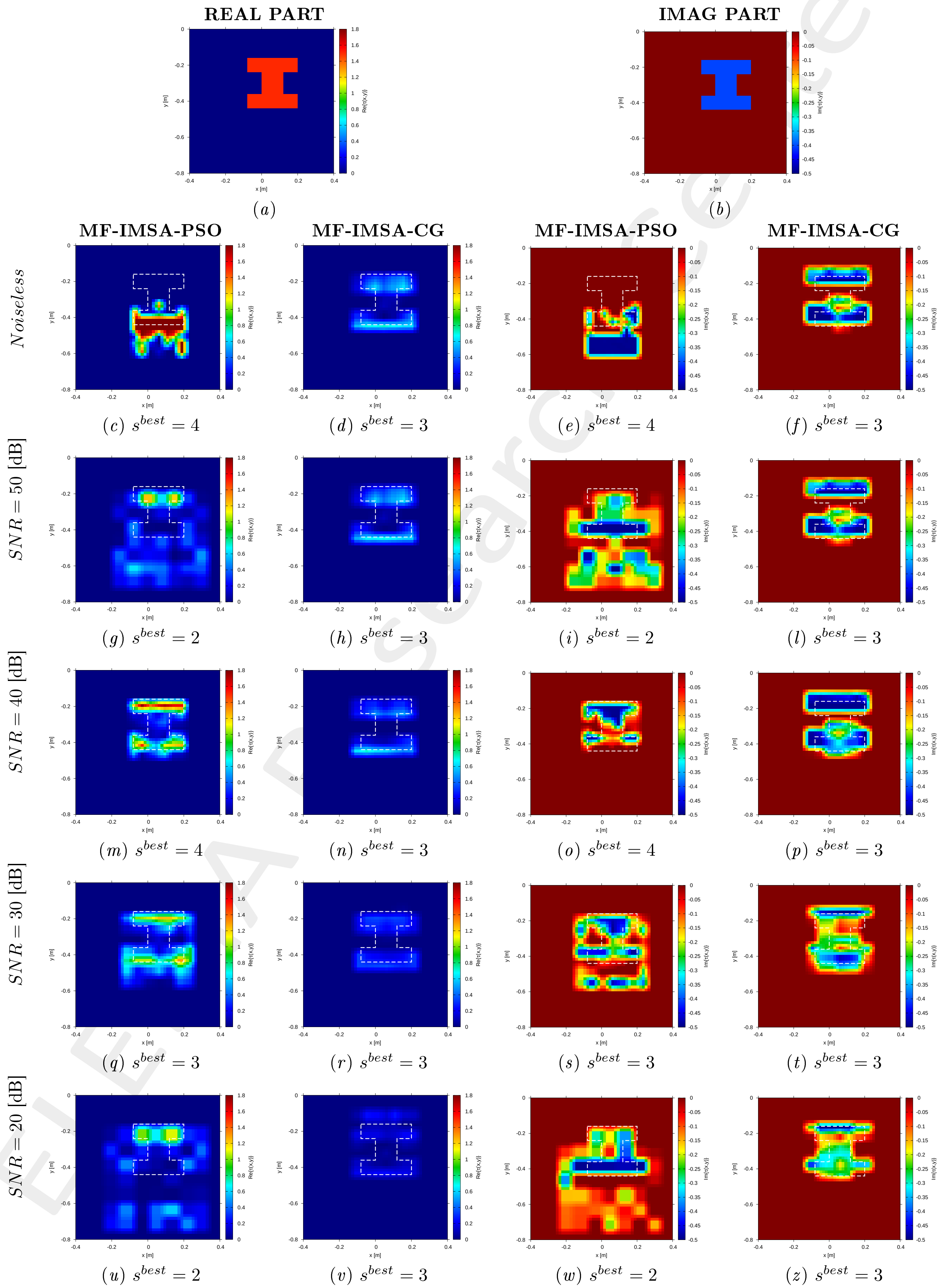

Figure 8: $MF-IMSA-PSO$ vs. $MF-IMSA-CG$: Retrieved dielectric profiles at the $IMSA$ convergence

2.1.7 $MF-IMSA-PSO$ vs. $MF-IMSA-CG$: Errors vs. σ_{obj}

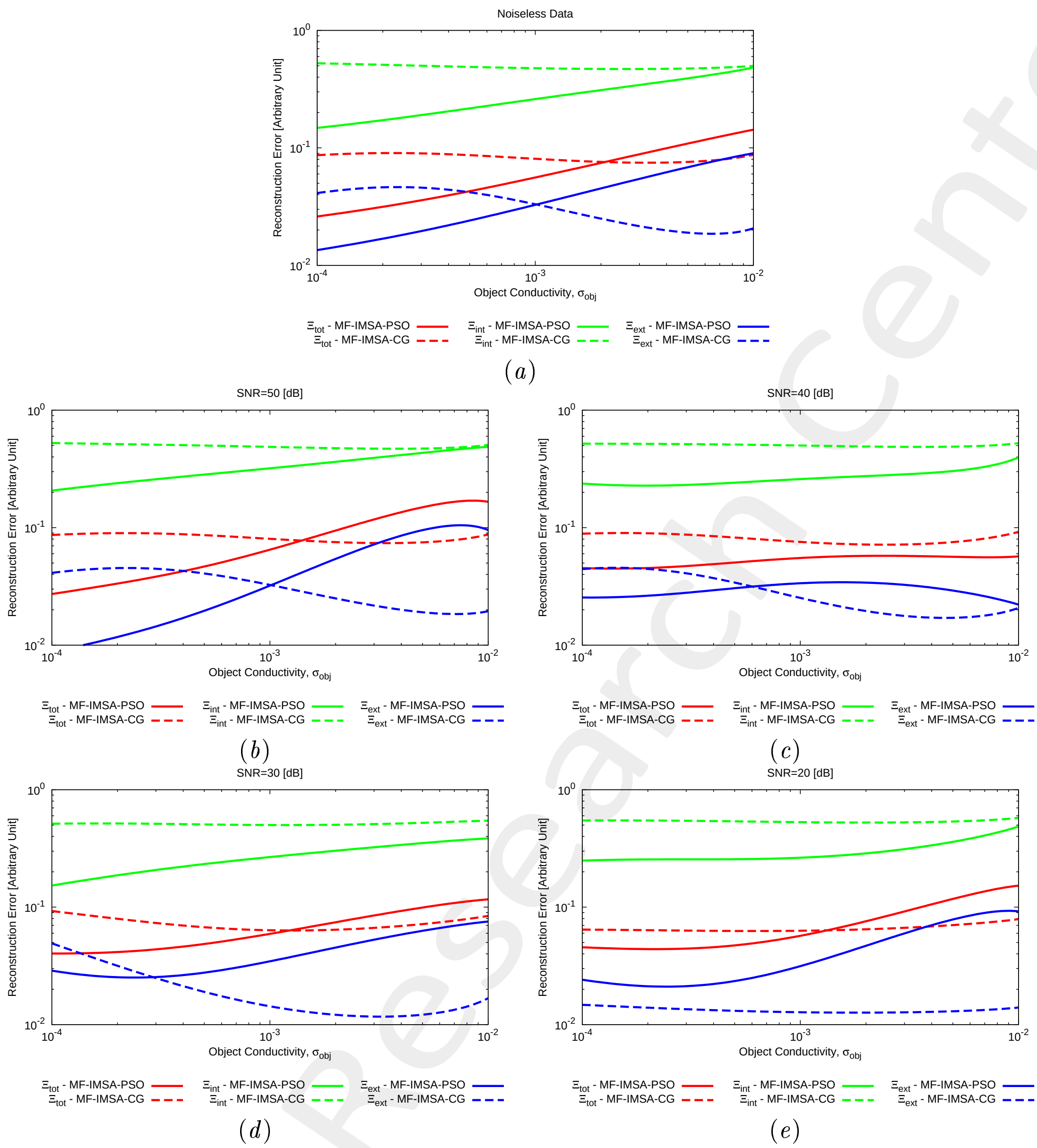

Figure 9: $MF-IMSA-PSO$ vs. $MF-IMSA-CG$: Reconstruction errors vs. the object conductivity (σ_{obj}).

2.1.8 $MF-IMSA-PSO$ vs. $MF-IMSA-CG$: Errors vs. SNR

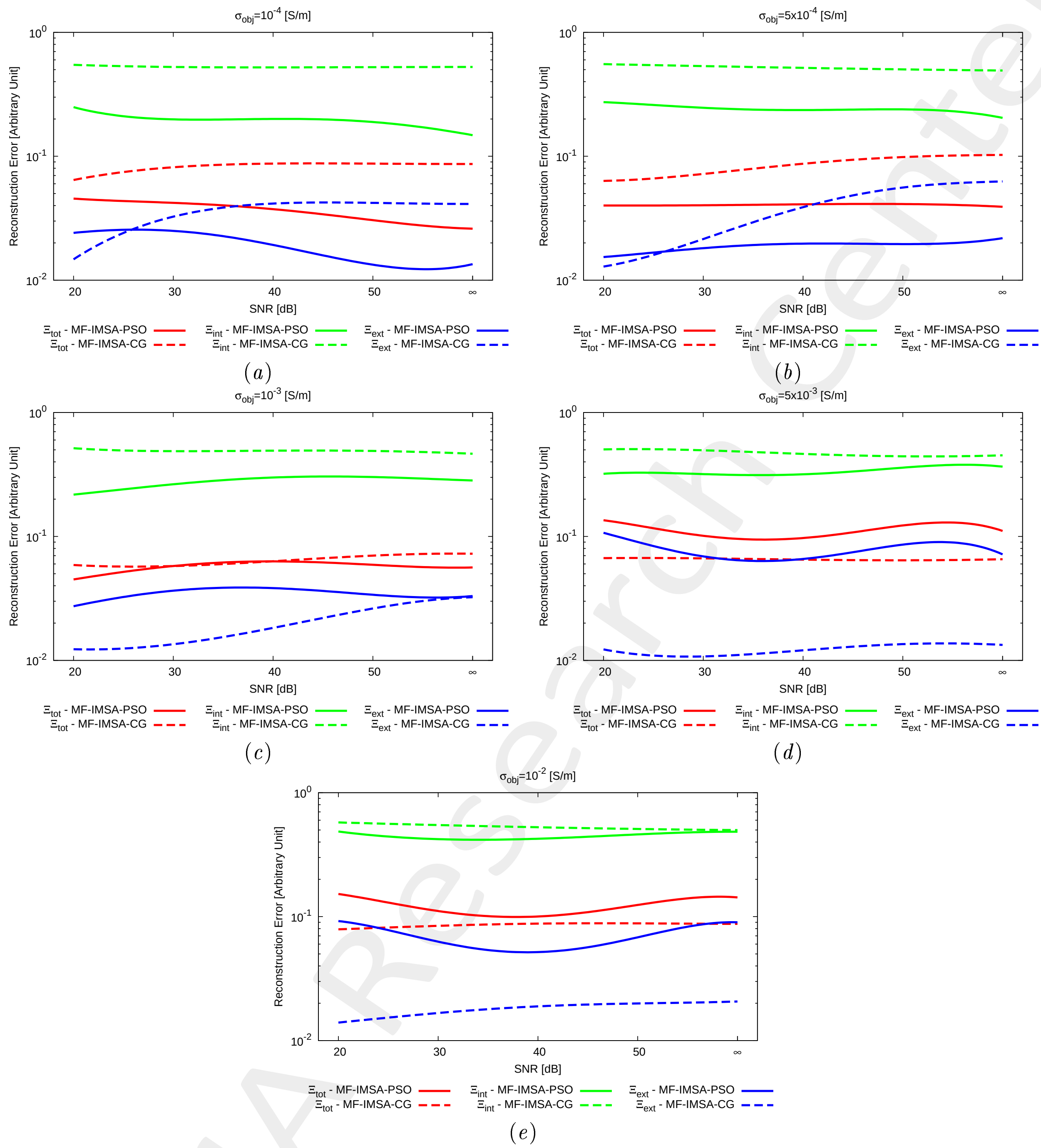

Figure 10: $MF-IMSA-PSO$ vs. $MF-IMSA-CG$: Reconstruction errors vs. SNR.

3 Conclusions

The reported results indicate that

- The proposed $MF{-}IMSA{-}PSO$ imaging technique yields accurate reconstructions also when considering a variation of the conductivity of the buried scatterer;
- On average a significant improvement of the retrieved profiles is obtained with respect to the $MF-IMSA-CG$ approach, which is based on a deterministic conjugate gradient (CG) solver [5].

References

[1] P. Rocca, M. Benedetti, M. Donelli, D. Franceschini, and A. Massa, "Evolutionary optimization as applied to inverse problems," *Inverse Probl.*, vol. 25, pp. 1-41, Dec. 2009.

[2] P. Rocca, G. Oliveri, and A. Massa, "Differential Evolution as applied to electromagnetics," *IEEE Antennas Propag. Mag.*, vol. 53, no. 1, pp. 38-49, Feb. 2011.

[3] M. Salucci, G. Oliveri, and A. Massa, "GPR prospecting through an inverse scattering frequency-hopping multi-focusing approach," *IEEE Trans. Geosci. Remote Sens.*, vol. 53, no. 12, pp. 6573-6592, Dec. 2015.

[4] M. Salucci, L. Poli, and A. Massa, "Advanced multi-frequency GPR data processing for non-linear deterministic imaging," *Signal Processing - Special Issue on 'Advanced Ground-Penetrating Radar Signal-Processing Techniques,'* vol. 132, pp. 306-318, Mar. 2017.

[5] M. Salucci, L. Poli, N. Anselmi and A. Massa, "Multifrequency particle swarm optimization for enhanced multiresolution GPR microwave imaging," *IEEE Trans. Geosci. Remote Sens.*, vol. 55, no. 3, pp. 1305-1317, Mar. 2017.

[6] A. Massa, P. Rocca, and G. Oliveri, "Compressive sensing in electromagnetics - A review," *IEEE Antennas Propag. Mag.*, pp. 224-238, vol. 57, no. 1, Feb. 2015.

[7] A. Massa and F. Texeira, Guest-Editorial: Special Cluster on Compressive Sensing as Applied to Electromagnetics, *IEEE Antennas Wireless Propag. Lett.*, vol. 14, pp. 1022-1026, 2015.

[8] N. Anselmi, G. Oliveri, M. Salucci, and A. Massa, "Wavelet-based compressive imaging of sparse targets," *IEEE Trans. Antennas Propag.*, vol. 63, no. 11, pp. 4889-4900, Nov. 2015.

[9] G. Oliveri, N. Anselmi, and A. Massa, "Compressive sensing imaging of non-sparse 2D scatterers by a total-variation approach within the Born approximation," *IEEE Trans. Antennas Propag.*, vol. 62, no. 10, pp. 5157-5170, Oct. 2014.

[10] T. Moriyama, G. Oliveri, M. Salucci, and T. Takenaka, "A multi-scaling forward-backward time-stepping method for microwave imaging," *IEICE Electron. Expr.*, vol. 11, no. 16, pp. 1-12, Aug. 2014.

[11] T. Moriyama, M. Salucci, M. Tanaka, and T. Takenaka, "Image reconstruction from total electric field data with no information on the incident field," *J. Electromagnet. Wave.*, vol. 30, no. 9, pp. 1162-1170, 2016.

[12] F. Viani, L. Poli, G. Oliveri, F. Robol, and A. Massa, "Sparse scatterers imaging through approximated multi-task compressive sensing strategies," *Microw. Opt. Technol. Lett.*, vol. 55, no. 7, pp. 1553-1557, Jul. 2013.

[13] M. Salucci, N. Anselmi, G. Oliveri, P. Calmon, R. Miorelli, C. Reboud, and A. Massa, "Real-time NDT-NDE through an innovative adaptive partial least squares SVR inversion approach," *IEEE Trans. Geosci. Remote Sens.*, vol. 54, no. 11, pp. 6818-6832, Nov. 2016.

[14] L. Poli, G. Oliveri, and A. Massa, "Imaging sparse metallic cylinders through a local shape function bayesian compressing sensing approach," *J. Opt. Soc. Am. A*, vol. 30, no. 6, pp. 1261-1272, Jun. 2013.

[15] M. Donelli, D. Franceschini, P. Rocca, and A. Massa, "Three-dimensional microwave imaging problems solved through an efficient multiscaling particle swarm optimization," *IEEE Trans. Geosci. Remote Sensing*, vol. 47, no. 5, pp. 1467-1481, May 2009.